A&A 462, 953–963 (2007)
DOI: 10.1051/0004-6361:20041577

Astronomy & Astrophysics

The abundance pattern of O, Mg, Si, and Fe in the intracluster medium of the Centaurus cluster observed with XMM-Newton

K. Matsushita[1,2], H. Böhringer[2], I. Takahashi[3], and Y. Ikebe[4]

[1] Department of Physics, Tokyo University of Science, 1-3 Kagurazaka, Shinjyuku-ku, Tokyo 162-8601, Japan
e-mail: matusita@rs.kagu.tus.ac.jp
[2] Max-Planck-Institut für Extraterrestrial Physik, 85748 Garching, Germany
[3] Department of Physics, University of Tokyo, 7-3-1 Hongo, Bunkyo-ku, Tokyo 113-8654, Japan,
[4] Joint Center for Astrophysics, University of Maryland, Baltimore County, 1000 Hilltop Circle, Baltimore, MD 21250, USA

Received 15 April 2003 / Accepted 9 October 2006

ABSTRACT

The abundances of O, Mg, Si, and Fe in the intracluster medium of the Centaurus cluster are derived. The Fe abundance has a negative radial gradient. In solar units, the Si abundance is close to the Fe abundance, while the O and Mg abundances are much lower. The high Fe/O and Si/O ratios indicate that the metal supply from supernovae Ia is important and that supernovae Ia synthesize Si as does Fe. Within 2′, the O and Mg abundances are consistent with the stellar metallicity of the cD galaxy derived from the Mg_2 index. This result indicates that the central gas is dominated by the gas from the cD galaxy. The observed abundance pattern of the Centaurus cluster resembles those observed in the center of other clusters and groups of galaxies. However, the central Fe abundance and the Si/Fe ratio are 40% higher and 30% lower than those of M 87, respectively. Since the accumulation timescale of the supernovae Ia is greater in the Centaurus cluster, these differences imply a time dependence of nucleosynthesis by the supernovae Ia.

Key words. X-rays: ISM – galaxies: ISM – galaxies: individual: Centaurus cluster

1. Introduction

The intracluster medium (ICM) contains a large amount of metals, which are synthesized by supernovae (SNe) Ia and SNe II in cluster galaxies. A knowledge of the contributions from the two types of SNe to the metal abundances is important for understanding the origin of the metals and for studying the evolution of galaxies in clusters.

The XMM-Newton observatory enables us to derive O and Mg abundances, which are not synthesized by SN Ia. For the ICM of M 87 observed with the XMM, the O/Si ratio is found to be about a half of the solar ratio, while Fe and Si have similar values in units of the solar abundance (Böhringer et al. 2001; Finoguenov et al. 2002; Matsushita et al. 2003). Such low O abundances compared to the Si abundances are also derived for the centers of other clusters and groups of galaxies (e.g. Tamura et al. 2001a; Boute et al. 2003, and others).

To account for the observed O/Si/Fe abundance pattern of M 87, the Fe/Si ratio of ejecta of SN Ia should be about 1 solar ratio. This value is significantly higher than expected and probably related to the dimmer SNe Ia observed in old stellar systems (Hamuy et al. 1996; Ivanov et al. 2000). Since the mass of synthesized Ni^{56} determines the luminosity of each SN, the abundance ratio in the ejecta may be correlated to the luminosity of SN Ia. In this context a lower Ni^{56} yield implies less complete nuclear burning with a higher ratio of α-elements such as Si to Fe. The observed O/Si/Fe pattern of the Galactic stars also indicates that the Si/Fe ratio in ejecta of SN Ia depends on stellar metallicity, i.e., age of the system (Matsushita et al. 2003).

The variation in the observed abundance pattern reflects variations in the explosion models, e.g. a high fraction of Fe for the classical deflagration model, W7 (Nomoto et al. 1984), or a larger fraction of Si for the delayed detonation model, WDDs (Nomoto et al. 1997; Iwamoto et al. 1999). The W7 model, which can reproduce observed optical spectra of SNe Ia well (Nugent et al. 1997), predicts a high Fe/Si ratio of 2.6 in units of the solar ratio. In contrast, the WDD models give a wider range of Fe/Si ratios from 1 to 3 in units of the solar ratio, which might be related to the age of the system (Umeda et al. 1999).

In this paper, we report on the O/Mg/Si/Fe abundance pattern of the Centaurus cluster observed with XMM. The temperature properties of the cluster are described in Takahashi (2004). The Centaurus cluster is a nearby cluster, centered on the cD galaxy, NGC 4696. A positive temperature gradient and a negative abundance gradient are observed with ASCA (Fukazawa et al. 1994; Ikebe et al. 1999). The cluster is expected to have a cooling flow (Allen & Fabian 1994), and Chandra observed an unusual plume-like cool structure at the center (Sanders & Fabian 2002). However, as in other cooling flow clusters, the luminosity of the central cool component is much lower than the expected value from the cooling flow model (e.g. Makishima et al. 2001; Tamura et al. 2001b; Böhringer et al. 2002; Matsushita et al. 2002). The problem of the missing the cooling component becomes an advantage when determining of elemental abundances, since the observed narrow temperature range of the ICM strongly reduces the ambiguity in the abundance measurement.

For the solar abundances we adopt the values given by Feldman (1992), where the solar Fe abundance relative to H is 3.24×10^{-5} in number. A value for the Hubble constant of $H_0 = 70$ km s^{-1}/Mpc is assumed. Unless otherwise specified, we use 90% confidence error regions.

Table 1. Results of the spectrum fitting of the projected spectra.

r (arcmin)			kT (keV)	(keV)	$N_{\rm H}$ (10^{20} cm^{-2})	O (solar)	Mg (solar)	Si (solar)	Fe (solar)	χ^2/d.o.f.
0.05–0.25	EMOS	1T	1.00		17.8	0.00	0.09	0.28	0.34	837/ 61
0.25–0.50	EMOS	1T	1.36		15.0	0.25	0.00	0.47	0.67	740/ 96
0.50–0.70	EMOS	1T	1.66		11.8	0.33	0.09	1.01	1.20	386/ 93
0.70–1.00	EMOS	1T	1.89		10.9	0.44	0.18	1.31	1.50	483/127
1.00–1.40	EMOS	1T	$2.42^{+0.05}_{-0.05}$		$9.4^{+0.6}_{-0.6}$	$0.64^{+0.19}_{-0.18}$	0.28	$1.60^{+0.17}_{-0.16}$	$2.04^{+0.13}_{-0.12}$	283/148
1.40–2.00	EMOS	1T	$2.77^{+0.05}_{-0.05}$		$8.8^{+0.5}_{-0.5}$	$0.50^{+0.17}_{-0.16}$	0.41	$1.58^{+0.15}_{-0.14}$	$1.83^{+0.09}_{-0.09}$	266/169
2.00–2.80	EMOS	1T	$3.00^{+0.05}_{-0.05}$		$8.8^{+0.4}_{-0.5}$	$0.70^{+0.17}_{-0.16}$	0.56	$1.43^{+0.14}_{-0.13}$	$1.66^{+0.08}_{-0.08}$	307/193
2.80–4.00	EMOS	1T	$3.32^{+0.06}_{-0.06}$		$9.2^{+0.4}_{-0.4}$	$0.60^{+0.15}_{-0.15}$	0.31	$0.98^{+0.12}_{-0.12}$	$1.14^{+0.06}_{-0.06}$	331/224
4.00–5.60	EMOS	1T	$3.60^{+0.07}_{-0.07}$		$8.2^{+0.4}_{-0.3}$	$0.37^{+0.14}_{-0.14}$	0.48	$0.78^{+0.11}_{-0.11}$	$0.80^{+0.05}_{-0.05}$	329/240
5.60–8.00	EMOS	1T	$3.71^{+0.10}_{-0.08}$		$8.0^{+0.4}_{-0.4}$	$0.49^{+0.15}_{-0.15}$	0.48	$0.70^{+0.11}_{-0.11}$	$0.68^{+0.05}_{-0.05}$	366/271
8.00–13.50	EMOS	1T	$3.75^{+0.12}_{-0.10}$		$7.3^{+0.4}_{-0.4}$	$0.43^{+0.14}_{-0.13}$	0.84	$0.62^{+0.11}_{-0.10}$	$0.57^{+0.05}_{-0.05}$	439/325
8.00–13.50	EMOS	2T	$4.30^{+1.68}_{-0.29}$	$1.43^{+0.76}_{-0.21}$	$7.3^{+0.3}_{-0.4}$	$0.44^{+0.07}_{-0.13}$	0.73	$0.65^{+0.12}_{-0.13}$	$0.53^{+0.08}_{-0.11}$	409/322
8.00–13.50	EMOS	14T			$9.3^{+1.2}_{-1.3}$	$0.33^{+0.16}_{-0.08}$	0.78	$0.66^{+0.09}_{-0.09}$	$0.57^{+0.04}_{-0.06}$	396/311
0.05–0.25	EPN	1T	0.78		28.8	0.01	0.00	0.09	0.14	1151/139
0.25–0.50	EPN	1T	1.37		12.5	0.00	0.00	0.45	0.71	1087/201
0.50–1.00	EPN	1T	1.89		8.7	0.04	0.00	0.98	1.48	1044/343
1.00–1.40	EPN	1T	$2.38^{+0.04}_{-0.04}$		$7.2^{+0.6}_{-0.7}$	$0.19^{+0.15}_{-0.13}$	0.00	$1.38^{+0.17}_{-0.13}$	$1.88^{+0.11}_{-0.08}$	476/313
1.40–2.00	EPN	1T	$2.70^{+0.04}_{-0.04}$		$7.2^{+0.5}_{-0.5}$	$0.25^{+0.13}_{-0.13}$	0.08	$1.29^{+0.14}_{-0.13}$	$1.68^{+0.08}_{-0.07}$	459/364
2.00–2.80	EPN	1T	$2.92^{+0.05}_{-0.04}$		$7.5^{+0.5}_{-0.6}$	$0.39^{+0.15}_{-0.13}$	0.09	$1.00^{+0.12}_{-0.11}$	$1.49^{+0.08}_{-0.06}$	579/412
2.80–4.00	EPN	1T	$3.25^{+0.05}_{-0.05}$		$7.3^{+0.5}_{-0.4}$	$0.06^{+0.11}_{-0.06}$	0.20	$0.82^{+0.11}_{-0.11}$	$1.06^{+0.05}_{-0.05}$	533/472
4.00–5.60	EPN	1T	$3.60^{+0.06}_{-0.04}$		$6.6^{+0.4}_{-0.4}$	$0.12^{+0.12}_{-0.12}$	0.01	$0.54^{+0.12}_{-0.12}$	$0.80^{+0.04}_{-0.04}$	591/496
5.60–8.00	EPN	1T	$3.84^{+0.07}_{-0.07}$		$6.1^{+0.4}_{-0.4}$	$0.05^{+0.12}_{-0.05}$	0.05	$0.40^{+0.11}_{-0.11}$	$0.65^{+0.04}_{-0.04}$	579/527
8.00–16.00	EPN	1T	$3.98^{+0.14}_{-0.05}$		$5.7^{+0.3}_{-0.5}$	$0.04^{+0.16}_{-0.04}$	0.00	$0.36^{+0.11}_{-0.09}$	$0.63^{+0.06}_{-0.03}$	805/687
8.00–16.00	EPN	2T	$4.14^{+0.17}_{-0.06}$	$1.06^{+0.08}_{-0.17}$	$6.2^{+0.4}_{-0.5}$	$0.24^{+0.14}_{-0.12}$	0.01	$0.44^{+0.11}_{-0.11}$	$0.66^{+0.05}_{-0.03}$	746/684
8.00–16.00	EPN	14T			$6.4^{+3.0}_{-0.4}$	$0.25^{+0.18}_{-0.13}$	0.00	$0.45^{+0.09}_{-0.10}$	$0.66^{+0.04}_{-0.05}$	736/674

2. Observation

The Centaurus cluster was observed with XMM-Newton on January 3rd, 2002. The thin filter was used for the EMOS and the EPN. We selected events with patterns smaller than 5 and 13 for the EPN and the EMOS, respectively. The background spectrum was calculated for each spectrum by integrating blank sky data in the same detector regions. Among deep sky observations collected with XMM, we selected the data with the most similar background to that of the Centaurus cluster, after screening background flare events in the data, following Katayama et al. (2004). The effective exposures of the EPN and the EMOS were 29 ks and 32 ks, respectively. The spectra were accumulated within rings, centered on the X-ray peak of the cluster. After subtracting the background and correcting for the effect of vignetting, deprojected spectra were calculated by assuming spherical symmetry. For the EPN spectra, the response matrix file and the auxiliary response file corresponding to each spectrum were calculated using SAS-v5.4.1. For the EMOS data, we used m1_thin1v9q20t5r6_all_15.rsp. The spectral analysis used the XSPEC_v11.2.0 package. For the EPN data, we used the spectral range from 0.5 to 7.3 keV, in order to discard strong instrumental lines around 8 keV. We fitted the EMOS data in the spectral range from 0.4 to 9.0 keV. At $r > 8'$, the energy range of 1.45–1.55 keV of the EMOS was discarded due to a strong instrumental line. Here, r is the projected radius from the X-ray peak. We also denote R as the deprojected or three-dimensional radius.

3. Spectral fit with the MEKAL model

The first step in the analysis was to fit the annular (projected) spectra with a single temperature MEKAL (e.g. Kaastra 1992; Liedahl et al. 1995) model, and the deprojected spectra with a single and two-temperature MEKAL model with photoelectric absorption. Abundances of C and N were fixed to 1 solar, and those of other elements were determined separately. The abundances of each element for all temperature components were assumed to have the same values. In addition, the deprojected spectra were fitted with a multi-temperature model, which is a sum of 14 temperature components. Since a spectrum from an isothermal plasma can be reproduced well by a sum of the spectra of plasma for two neighboring temperatures with similar elemental abundances, we selected temperatures to derive metal abundances with an accuracy within 5%. Thus, in order to determine the abundance distribution, this multi-temperature model is enough to fit any temperature distribution, at least when all temperature components have the same abundances.

Tables 1 and 2 summarize the results. Even for the deprojected spectra, the single-temperature model is not acceptable at $R < 2'$. The two-temperature model dramatically reduces the χ^2, and the multi-temperature model slightly improves χ^2. Outside this radius, χ^2 derived from the two- and the multi-temperature models are slightly smaller than those of the single-temperature model. Figure 1 shows a representative spectrum for $R = 0.5-2'$. Using the two- and the multi-temperature MEKAL models, not only the continuum and the Fe-L bump, but also the strength of the Fe-K line is fitted well. The consistency between the Fe-L and the Fe-K will be discussed in detail in Sect. 4.3.3. A residual structure remains around 1.2−1.5 keV in the Fe-L/Mg-K region. Therefore, in Tables 1 and 2, we do not show errors in the Mg abundances.

The temperature of the ICM decreases sharply toward the center (Fig. 2), and we need more than two-temperature components to fit the deprojected spectra in the central region. The observed sharp temperature gradient means that the

Table 2. Results of the spectrum fitting of the deprojected spectra.

R (arcmin)			$kT1$ (keV)	$kT2$ (keV)	$N_{\rm H}$ (10^{20} cm^{-2})	O (solar)	Mg (solar)	Si (solar)	Fe (solar)	χ^2/d.o.f.
0.00–0.50	EMOS	1T	1.08		15.9	0.17	0.11	0.35	0.45	1111/129
0.00–0.50	EMOS	2T	$1.51^{+0.05}_{-0.07}$	$0.71^{+0.01}_{-0.02}$	$11.4^{+2.4}_{-1.1}$	$0.49^{+0.18}_{-0.18}$	0.89	$1.30^{+0.23}_{-0.30}$	$1.57^{+0.24}_{-0.28}$	169/126
0.00–0.50	EMOS	14T			$11.4^{+3.7}_{-2.1}$	$0.48^{+0.25}_{-0.19}$	0.89	$1.39^{+0.46}_{-0.33}$	$1.79^{+0.42}_{-0.34}$	139/116
0.00–0.50	EPN	1T	0.97		16.9	0.14	0.04	0.28	0.38	1167/176
0.00–0.50	EPN	2T	$1.45^{+0.07}_{-0.08}$	$0.70^{+0.02}_{-0.02}$	$11.6^{+1.2}_{-2.4}$	$0.59^{+0.29}_{-0.19}$	0.80	$1.52^{+0.45}_{-0.38}$	$1.85^{+0.29}_{-0.35}$	195/173
0.00–0.50	EPN	14T			$20.8^{+12.9}_{-7.5}$	$0.71^{+0.37}_{-0.28}$	1.39	$2.48^{+0.74}_{-1.00}$	$3.44^{+0.74}_{-1.26}$	170/163
0.50–1.00	EMOS	1T	1.43		13.5	0.49	0.24	1.20	1.17	354/146
0.50–1.00	EMOS	2T	$1.74^{+0.07}_{-0.03}$	$0.85^{+0.03}_{-0.04}$	$9.7^{+1.3}_{-1.6}$	$1.15^{+0.45}_{-0.30}$	1.26	$2.79^{+0.72}_{-0.42}$	$2.71^{+0.57}_{-0.33}$	189/143
0.50–1.00	EMOS	14T			$9.3^{+1.2}_{-1.6}$	$1.22^{+0.47}_{-0.33}$	1.43	$3.06^{+0.72}_{-0.62}$	$2.93^{+0.56}_{-0.75}$	189/133
1.00–2.00	EMOS	1T	$2.30^{+0.06}_{-0.05}$		$8.8^{+0.8}_{-0.8}$	$0.49^{+0.22}_{-0.20}$	0.34	$1.83^{+0.22}_{-0.20}$	$2.22^{+0.18}_{-0.16}$	246/212
1.00–2.00	EMOS	2T	$2.46^{+0.25}_{-0.12}$	$1.30^{+0.31}_{-0.37}$	$8.7^{+0.8}_{-0.8}$	$0.62^{+0.24}_{-0.22}$	0.53	$2.07^{+0.27}_{-0.25}$	$2.42^{+0.23}_{-0.20}$	220/209
1.00–2.00	EMOS	14T			$8.6^{+1.0}_{-0.8}$	$0.62^{+0.25}_{-0.21}$	0.58	$2.12^{+0.28}_{-0.26}$	$2.44^{+0.22}_{-0.21}$	214/199
0.50–2.00	EMOS	1T	1.95		10.2	0.40	0.20	1.42	1.70	658/249
0.50–2.00	EMOS	2T	$2.20^{+0.07}_{-0.05}$	$1.00^{+0.12}_{-0.08}$	$9.0^{+0.6}_{-0.6}$	$0.78^{+0.16}_{-0.16}$	0.79	$2.23^{+0.20}_{-0.20}$	$2.46^{+0.16}_{-0.16}$	339/246
0.50–2.00	EMOS	14T			$8.9^{+0.6}_{-0.7}$	$0.78^{+0.17}_{-0.15}$	0.80	$2.33^{+0.21}_{-0.21}$	$2.54^{+0.16}_{-0.17}$	322/236
0.50–2.00	EPN	1T	2.10		7.6	0.08	0.00	1.24	1.73	1074/458
0.50–2.00	EPN	2T	$2.21^{+0.03}_{-0.03}$	$0.92^{+0.05}_{-0.07}$	$7.9^{+0.5}_{-0.6}$	$0.45^{+0.13}_{-0.09}$	0.19	$1.70^{+0.16}_{-0.10}$	$2.24^{+0.14}_{-0.07}$	649/455
0.50–2.00	EPN	14T			$8.0^{+0.4}_{-0.5}$	$0.46^{+0.11}_{-0.10}$	0.17	$1.68^{+0.13}_{-0.13}$	$2.14^{+0.12}_{-0.09}$	634/445
2.00–4.00	EMOS	1T	$2.94^{+0.06}_{-0.06}$		$9.5^{+0.6}_{-0.5}$	$0.78^{+0.20}_{-0.19}$	0.33	$1.42^{+0.16}_{-0.15}$	$1.72^{+0.10}_{-0.09}$	342/294
2.00–4.00	EMOS	2T	$5.30^{+4.35}_{-2.14}$	$2.42^{+0.31}_{-0.89}$	$9.4^{+0.6}_{-0.5}$	$0.72^{+0.19}_{-0.18}$	0.39	$1.39^{+0.16}_{-0.15}$	$1.63^{+0.13}_{-0.11}$	324/291
2.00–4.00	EMOS	14T			$9.3^{+0.9}_{-0.4}$	$0.78^{+0.20}_{-0.20}$	0.44	$1.45^{+0.15}_{-0.18}$	$1.67^{+0.09}_{-0.12}$	319/281
2.00–4.00	EPN	1T	$2.84^{+0.05}_{-0.05}$		$7.7^{+0.7}_{-0.7}$	$0.26^{+0.17}_{-0.16}$	0.22	$1.15^{+0.17}_{-0.15}$	$1.56^{+0.09}_{-0.08}$	491/463
2.00–4.00	EPN	2T	37(>5.0)	$2.74^{+0.08}_{-0.07}$	$7.8^{+0.6}_{-0.8}$	$0.25^{+0.16}_{-0.15}$	0.18	$1.13^{+0.19}_{-0.13}$	$1.54^{+0.11}_{-0.07}$	472/460
2.00–4.00	EPN	14T			$8.3^{+1.7}_{-0.9}$	$0.34^{+0.17}_{-0.19}$	0.19	$1.11^{+0.18}_{-0.14}$	$1.48^{+0.10}_{-0.08}$	479/450
4.00–8.00	EMOS	1T	$3.54^{+0.11}_{-0.09}$		$8.9^{+0.6}_{-0.5}$	$0.43^{+0.20}_{-0.19}$	0.34	$0.78^{+0.15}_{-0.14}$	$0.83^{+0.07}_{-0.06}$	391/332
4.00–8.00	EMOS	2T	$6.32^{+7.99}_{-4.15}$	$2.76^{+0.55}_{-0.58}$	$8.8^{+0.6}_{-0.6}$	$0.41^{+0.19}_{-0.18}$	0.32	$0.76^{+0.15}_{-0.14}$	$0.80^{+0.10}_{-0.09}$	377/329
4.00–8.00	EMOS	14T			$9.1^{+1.0}_{-0.7}$	$0.41^{+0.18}_{-0.18}$	0.35	$0.78^{+0.16}_{-0.14}$	$0.80^{+0.09}_{-0.07}$	377/319
4.00–8.00	EPN	1T	$3.56^{+0.10}_{-0.10}$		$6.4^{+0.8}_{-0.6}$	$0.03^{+0.20}_{-0.03}$	0.33	$0.58^{+0.18}_{-0.17}$	$0.82^{+0.07}_{-0.06}$	541/534
4.00–8.00	EPN	2T	$3.57^{+0.12}_{-0.09}$	$0.84^{+0.53}_{-0.36}$	$6.9^{+0.8}_{-0.9}$	$0.12^{+0.27}_{-0.12}$	0.36	$0.60^{+0.21}_{-0.16}$	$0.83^{+0.11}_{-0.06}$	536/531
4.00–8.00	EPN	14T			$6.9^{+1.5}_{-0.9}$	$0.15^{+0.22}_{-0.15}$	0.38	$0.62^{+0.17}_{-0.17}$	$0.82^{+0.07}_{-0.07}$	535/521
2.00–8.00	EMOS	1T	$3.26^{+0.06}_{-0.05}$		$9.3^{+0.3}_{-0.3}$	$0.55^{+0.12}_{-0.12}$	0.33	$0.99^{+0.09}_{-0.09}$	$1.14^{+0.05}_{-0.05}$	539/387
2.00–8.00	EMOS	2T	$6.17^{+2.56}_{-1.11}$	$2.60^{+0.28}_{-0.24}$	$9.2^{+0.3}_{-0.3}$	$0.52^{+0.11}_{-0.11}$	0.32	$0.97^{+0.08}_{-0.08}$	$1.10^{+0.07}_{-0.06}$	495/384
2.00–8.00	EMOS	14T			$9.2^{+0.6}_{-0.3}$	$0.52^{+0.13}_{-0.11}$	0.34	$0.98^{+0.08}_{-0.09}$	$1.08^{+0.05}_{-0.05}$	502/374
2.00–8.00	EPN	1T	$3.23^{+0.08}_{-0.02}$		$7.1^{+0.3}_{-0.7}$	$0.13^{+0.13}_{-0.13}$	0.28	$0.83^{+0.17}_{-0.10}$	$1.15^{+0.06}_{-0.03}$	825/686
2.00–8.00	EPN	2T	$3.18^{+0.05}_{-0.04}$	$0.86^{+0.37}_{-0.22}$	$7.6^{+0.4}_{-0.7}$	$0.19^{+0.17}_{-0.10}$	0.27	$0.82^{+0.15}_{-0.08}$	$1.12^{+0.07}_{-0.03}$	809/684
2.00–8.00	EPN	14T			$7.7^{+0.7}_{-1.0}$	$0.22^{+0.13}_{-0.14}$	0.26	$0.80^{+0.06}_{-0.09}$	$1.05^{+0.07}_{-0.04}$	801/674

single-temperature model is not enough to fit each deprojected spectrum, even if the ICM is isothermal locally. In addition, the cluster is not circularly symmetric and the cool plume-like structure at the center (Sanders & Fabian 2002) might introduce an additional temperature component.

The hydrogen column density, $N_{\rm H}$, is consistent with the Galactic value at $R > 1'$, although the EPN and the EMOS give slightly different results of a few times 10^{20} cm^{-2} (Fig. 2). Within $R < 1'$, the two- and the multi-temperature models give similar values to those of $R > 1'$. Higher column densities derived from the single temperature model within $R < 1'$ are not acceptable due to their high χ^2. Therefore, $N_{\rm H}$ is consistent with the Galactic value within the whole field of view.

Discarding the results of unacceptable fits (reduced $\chi^2 > 2$), the Fe abundance is ∼0.6 solar at $R > 8'$, and within the radius, it increases steeply toward center. Within $2'$, the gradient becomes weaker. The average value of the Fe abundance at $R < 2'$ is 2.3 solar (Fig. 3). The EPN and the EMOS give consistent Fe abundances within 10% (Table 2). The Fe abundances from the deprojected spectra are slightly higher than those from the projected spectra.

At each radius, the Si abundance is close to the Fe abundance (Figs. 3, 4). The uncertainties in the Si/Fe ratio are better constrained than those in the Si and Fe abundances themselves (Fig. 4), since the derived abundances for Si and Fe are correlated to each other. On average, the Si/Fe ratio is 0.89 ± 0.04 and 0.75 ± 0.04 in units of the solar ratio using the EMOS and EPN, respectively.

The O abundances are much lower than the Si and Fe abundances (Figs. 3, 4). The two detectors give inconsistent O abundances. Using the EMOS, the O abundance is about 0.8 solar at $R = 0.5$–$2.0'$ and at $R > 2'$, it reduces to 0.4 solar (Fig. 3), and the O/Fe ratio increases toward outer regions (Fig. 4). In contrast, the EPN gives a significantly smaller O abundance than the EMOS especially in the outer regions (Fig. 3), and the profile of the O/Fe ratio is consistent with no radial gradient (Fig. 4).

As in center of other clusters and groups of galaxies, the Fe and Si abundances are close to each other with strong negative radial gradients. The O abundance is at least a factor of 2 lower. The discrepancies in the O and Si abundances between the EMOS and EPN is discussed in Sect. 4.3.1.

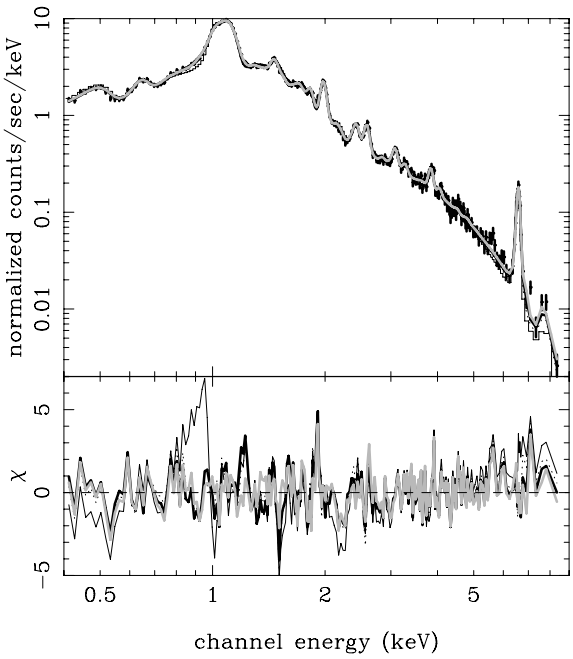

Fig. 1. The deprojected spectrum at $R = 0.5-2'$ of the EMOS1+EMOS2 of the Centaurus cluster fitted with the single-temperature MEKAL model (black thin lines), the two-temperature MEKAL model (black dotted lines), the multi-temperature MEKAL model (black bold lines), and the multi-temperature APEC model (gray bold lines).

4. Uncertainties in the abundance determination

In the abundance determination, we must examine uncertainties such as the dependence on the plasma code and on the background subtraction. In this section, we study these uncertainties and also calibrate the abundances with the strengths of the lines.

4.1. The effect of the plasma code

To constrain the effect of the plasma code on the abundance determination, we compared the results from the APEC (Smith et al. 2001) model with those from the MEKAL model. We used the APEC version 1.1 model in XSPEC version 11.2. As in the MEKAL model fit, we fitted the deprojected spectra with a single and a multi-temperature APEC model.

The results are summarized in Table 3. With the APEC model, the fit to the Fe-L/Mg-K region at 1.2−1.5 keV improved from that with the MEKAL code (Fig. 1). As a result, the reduced χ^2 are consistent or slightly smaller than those from the MEKAL model fit. The derived temperatures, hydrogen column densities, and the Si and Fe abundances are consistent within 10% to those from the MEKAL code (Figs. 5, 6).

However, the O and the Mg abundances increased by ∼20% and ∼80%, respectively, from the MEKAL model fit. The difference in the O abundance is consistent with the difference in the strength of the H-like O line between the APEC and MEKAL models, since at 2 keV, the strength of APEC is 10% greater than for the MEKAL model, and at 4 keV, the difference increases to 30%. The difference in the Mg abundance is not due to the difference in the strength of the Mg-K line between the two codes, which is smaller than for O below 4 keV. It should be caused by the difference in the Fe-L modeling around the Mg-K line. We discuss this in Sect. 4.3.2.

4.2. Effect of the background uncertainty

One of the biggest problems in analyzing XMM-Newton data are uncertainties in the background. In this paper, we adopted deep survey data as a background, which agrees well with the data of the Centaurus cluster above 8 keV (Fig. 7). In addition, to study the effect of the uncertainty of the background, we artificially scaled the background by 10% and fitted the projected EMOS spectra at $r > 2'$ in the same way as previously. Since spectral variations in the background amount to about 10% below 1 keV when the background is scaled with the count-rate outside the field of the view of the detector (Katayama et al. 2004), and the relatively high Galactic $N_{\rm H}$ towards the Centaurus cluster absorbs the low energy photons from the cosmic X-ray background (CXB).

The results are summarized in Fig. 8. Within 8′, the derived temperatures, the Fe abundances, the O/Fe, and the Si/Fe ratios are consistent within a few % with those derived from the background used in Sect. 3.1. Outside 8′, the 10% change of the background changes derived parameters by ∼10%. Therefore, the background problem is not acute in this observation.

4.3. Comparisons between the line strength and model fit

4.3.1. The line strengths of O and Si and the abundance determination

In order to study the discrepancy in the O and the Si abundances between the EMOS and the EPN data, it is important to check their line strengths directly. Complications arise since the energy resolution of the EMOS has become worse due to the radiation damage in orbit (Kirsh 2002), and that of the EPN depends on the distance from the read-out. In addition, there are still discrepancies of several % in the response matrix between the EPN and EMOS, which might give a large uncertainty in the strengths of weak lines.

The strengths of Kα lines of H-like O and Si were derived from fittings of the spectra around the lines with Gaussians. The details are the same as in Matsushita et al. (2003). First, the line widths of the Gaussians were frozen to zero, and then allowed to be free. Figure 9 compares the best-fit MEKAL model and the Gaussian fits for representative spectra at $R = 2-8'$. In the EMOS spectrum, we can see a weak bump on the H-like O line, and a clear bump on the H-like Si line. In contrast, in the spectrum of the EPN, with a worse energy resolution than does the EMOS, the continuum and the O line are hardly distinguished and the Si line is much broader than the EMOS one.

For the EMOS spectra, the line strengths of K_α of H-like O and Si from the Gaussian fits are consistent within 10% with those from the MEKAL model, except for the O line strength within 0.5′, where the O line is completely hidden in the Fe-L lines (Fig. 10). This result indicates that the effect of the decrease in the energy resolution of the EMOS detector should not affect the derived O and Si abundances.

In contrast, allowing the line width to be a free parameter, the Gaussian fits to the EPN spectra give systematically larger line strengths than the MEKAL model fit. As a result, adopting the values from the Gaussian fits, the EPN abundances become consistent with the EMOS ones. Therefore, the O and Si abundances derived from the EMOS fit should be reliable, since it has a better spectral resolution and it gives consistent strengths for the Kα lines between the Gaussian fits and the MEKAL model fits.

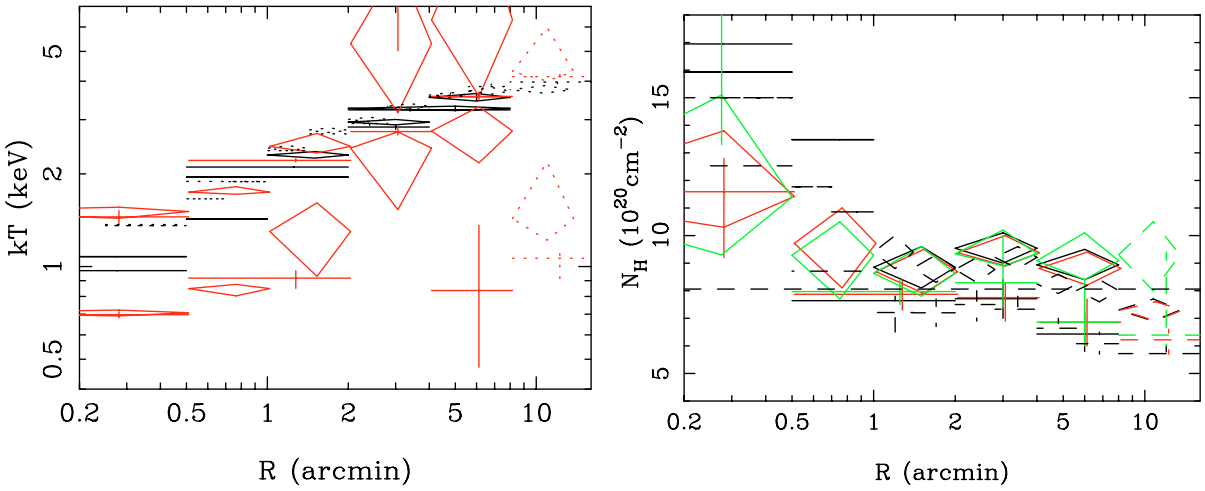

Fig. 2. The radial profiles of the temperature and the hydrogen column density. Dotted and solid lines correspond to the results of the projected spectra and the deprojected spectra, respectively. Black, red, and green correspond to the single, two, and the multi-temperature MEKAL model, respectively. The results from the EMOS are shown in diamonds and those from the EPN are shown in crosses. The dashed horizontal line in the profile of the hydrogen column density represents the Galactic value.

Table 3. Results of the spectrum fitting of the deprojected spectra within 8′ and the projected spectrum at 8−13.5′ of the EMOS with the single- and the multi-temperature APEC model.

R (arcmin)			kT (keV)	N_H (10^{20} cm^{-2})	O (solar)	Mg (solar)	Si (solar)	Fe (solar)	χ^2/d.o.f.
0.00–0.50	EMOS	1T	1.00	17.1	0.36	0.23	0.39	0.27	676/129
0.00–0.50	EMOS	14T		$10.6^{+2.7}_{-1.5}$	$0.50^{+0.23}_{-0.21}$	$1.45^{+0.49}_{-0.49}$	$1.47^{+0.34}_{-0.40}$	$1.72^{+0.19}_{-0.36}$	146/116
0.50–2.00	EMOS	1T	1.93	11.1	0.47	0.68	1.35	1.61	585/249
0.50–2.00	EMOS	14T		$9.3^{+0.6}_{-0.7}$	$0.91^{+0.21}_{-0.19}$	$1.54^{+0.15}_{-0.24}$	$2.29^{+0.25}_{-0.20}$	$2.42^{+0.20}_{-0.16}$	266/236
2.00–4.00	EMOS	1T	$2.94^{+0.06}_{-0.06}$	$9.8^{+0.6}_{-0.5}$	$0.96^{+0.27}_{-0.25}$	$0.89^{+0.28}_{-0.27}$	$1.46^{+0.17}_{-0.16}$	$1.83^{+0.11}_{-0.10}$	346/294
2.00–4.00	EMOS	14T		$9.5^{+0.7}_{-0.6}$	$1.00^{+0.26}_{-0.25}$	$0.89^{+0.28}_{-0.25}$	$1.49^{+0.19}_{-0.16}$	$1.76^{+0.13}_{-0.12}$	301/281
4.00–8.00	EMOS	1T	$3.53^{+0.11}_{-0.11}$	$9.1^{+0.6}_{-0.5}$	$0.61^{+0.27}_{-0.26}$	$0.62^{+0.31}_{-0.30}$	$0.84^{+0.16}_{-0.16}$	$0.92^{+0.08}_{-0.08}$	397/332
4.00–8.00	EMOS	14T		$9.1^{+0.5}_{-0.7}$	$0.54^{+0.27}_{-0.23}$	$0.58^{+0.32}_{-0.28}$	$0.84^{+0.18}_{-0.15}$	$0.88^{+0.10}_{-0.08}$	372/319
8.00–13.50	EMOS	1T	$3.77^{+0.10}_{-0.10}$	$7.4^{+0.4}_{-0.4}$	$0.52^{+0.18}_{-0.18}$		$0.67^{+0.12}_{-0.11}$	$0.63^{+0.06}_{-0.06}$	443/325
8.00–13.50	EMOS	14T		$8.7^{+1.1}_{-1.1}$	$0.38^{+0.18}_{-0.16}$		$0.72^{+0.13}_{-0.12}$	$0.60^{+0.08}_{-0.07}$	388/312

As shown in the Fig. 11, the ratio of the strengths of Kα lines for H-like O and Si becomes constant above 1.7 keV and increases toward lower energies. This temperature dependence means that any temperature distribution cannot yield an O/Si ratio higher than 0.6 solar within 4′. Furthermore, we got a higher value for the line ratio at $R > 8'$ by a factor of 2. It implies that the O/Si ratio increases in the region, since the contribution to the O line from the component below 1.7 keV of the multi-temperature MEKAL model is smaller than 10%.

4.3.2. The line strength of the Mg-K

It is also important to derive the strengths of the Kα-lines of Mg directly, since the Mg abundances derived from the spectral fits depend on modeling the underlying Fe-L lines. We therefore fitted the EMOS spectra within the energy range of 1.3−1.65 keV with Gaussians, plus one-, two-, or three-temperature MEKAL or APEC models.

All of the Gaussian models can fit the spectra around the Mg-K/Fe-L region well (Fig. 12). The derived strengths of the Kα-line of H-like and He-like Mg do not depend on the temperature structure (i.e. one-, two, or three-temperature models) or on the plasma code (i.e. MEKAL or APEC model). The line strengths agree well with those derived from fitting the spectra described in Sect. 4.1, but are systematically higher than those derived from the multi-temperature MEKAL model described in Sect. 3, which cannot reproduce the spectra around the Mg-K/Fe-L region (Fig. 13). Therefore, it is reasonable to adopt the Mg abundances derived from the multi-temperature APEC model fit as the Mg abundances of the ICM.

We note that the Mg/O ratio does not depend on the temperature structure since the line ratio of the Kα lines for these two elements is nearly constant above 1.1 keV (Matsushita et al. 2003).

4.3.3. The line strength of Fe-K

Since the temperature dependence on the intensities of the Fe-L and Fe-K lines is completely different, a comparison between the Fe-L and the Fe-K lines strongly constrains the temperature structure and the Fe abundance. In the spectral fitting by the MEKAL model or the APEC model, the strengths of the 6.7 keV Fe-K lines are fitted well, although the fit to the Fe-L lines mostly determines the Fe abundance due to its high statistics (Fig. 14).

When the Fe abundance is shifted by 40% in the fits with the multi-temperature model, the Fe-L structure can be roughly fitted, although the χ^2 increases significantly (Fig. 14). However, the strengths of the Fe-K line cannot be reproduced. Therefore, the uncertainties in the Fe-L line fit should not be severe

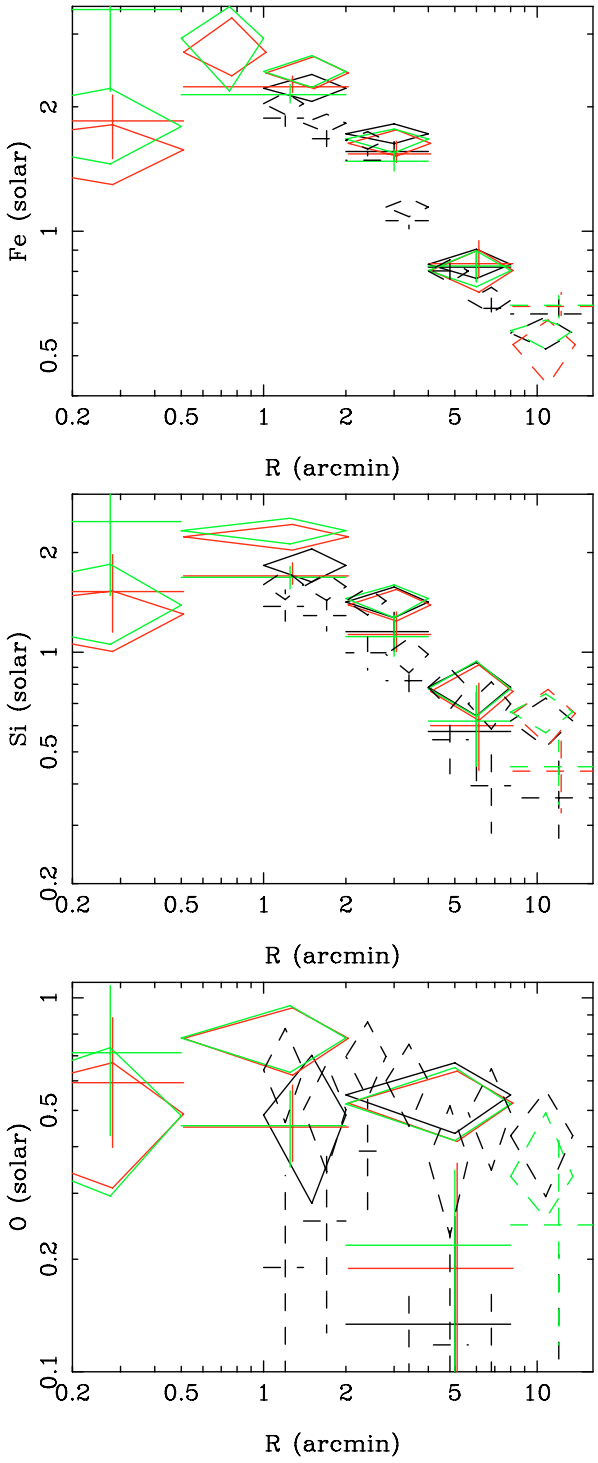

Fig. 3. Radial profiles of the abundances of Fe, Si and O. The meanings of symbols are the same as those in Fig. 2. The data with a reduced $\chi^2 > 2$ are not shown.

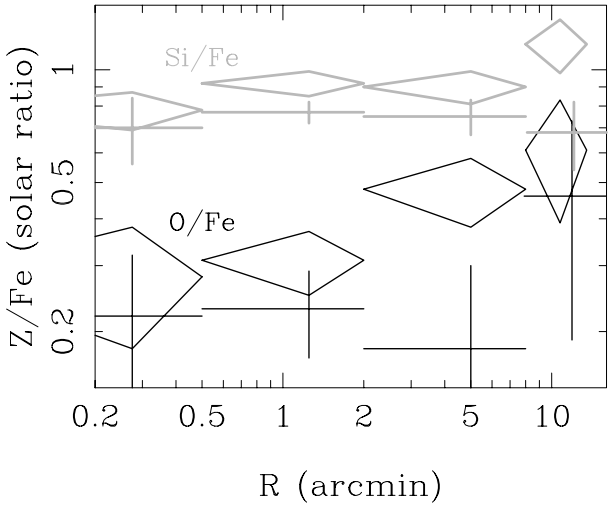

Fig. 4. Radial profiles of the O/Fe (black lines) and the Si/Fe (gray lines) ratios in units of the solar elemental ratio derived from the multi-temperature MEKAL model of the EMOS (diamonds) and the EPN (crosses) spectra.

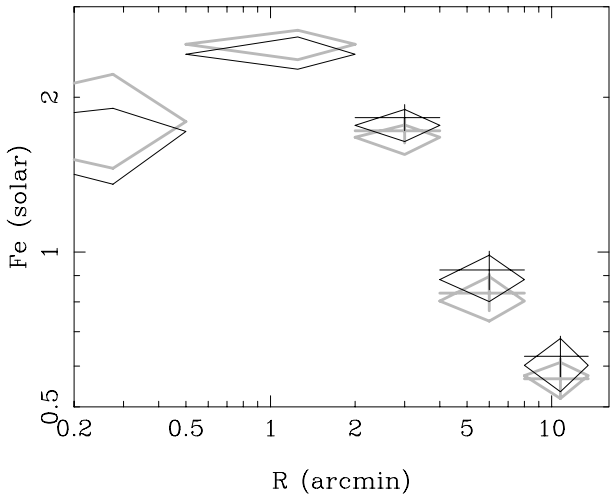

Fig. 5. The Fe abundance profile derived from the MEKAL (gray data) and the APEC (black data) models, from the single-temperature model (crosses), and the multi-temperature model (diamonds). The data with a reduced $\chi^2 > 2$ are not shown.

problems caused by the temperature structure and the plasma code in the Centaurus cluster.

Since abundances derived from the Fe-K line may have an uncertainty due to uncertainty in the background, we also derived the line strength of the Fe-K line directly from a Gaussian fit. The width of the Gaussian was allowed to be a free parameter, since the 6.7 keV Fe-K consists of several strong lines. In Fig. 15, the derived line strengths from the Gaussian fit are compared to the line strengths of the Fe-K line derived from the best-fit multi-temperature MEKAL model. These values agree within 10%. Thus, the line strengths of the Fe-K line are consistent with the Fe abundances derived from the MEKAL model fit, and a change in the Fe abundance cannot reproduce the observed line strength of the Fe-K.

5. Discussion

The abundances of O, Mg, Si, and Fe in the ICM of the Centaurus cluster were derived, and we checked for uncertainties in the temperature structure, in the background subtraction, and in the spectral model and studied their effects on the abundance determination. The Fe abundance is ~2.3 solar within 2′, and it decreases to ~0.6 solar at $R > 8'$. The Si abundance is close to the Fe abundance. In contrast, the O and Mg abundances are much lower than the Fe and Si abundances in units of the solar ratio.

The abundance pattern of the ICM of the Centaurus cluster, the low O abundance compared to those of Si and Fe, resembles

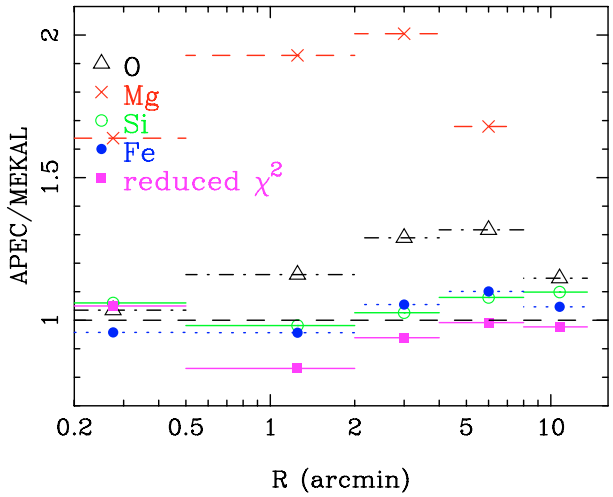

Fig. 6. The ratio of the O (open triangles), Mg (crosses), Si (open circles), and Fe (closed circles) abundances and the reduced χ^2 (closed boxes) between the multi-temperature APEC and the multi-temperature MEKAL models.

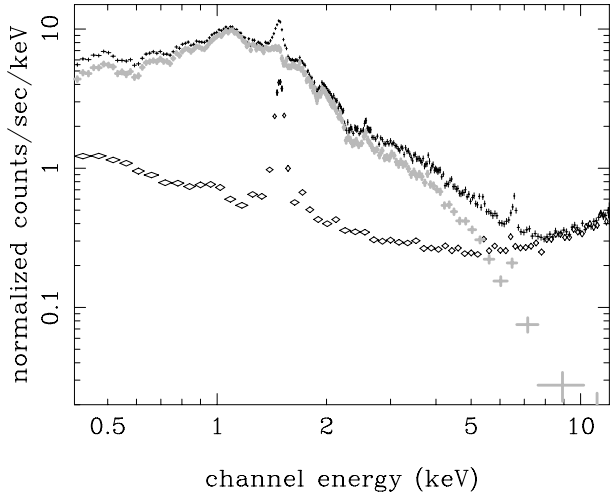

Fig. 7. The raw EMOS spectrum at $r > 8'$ (black crosses), the adopted background spectrum (black diamonds), and the background subtracted spectrum (gray crosses).

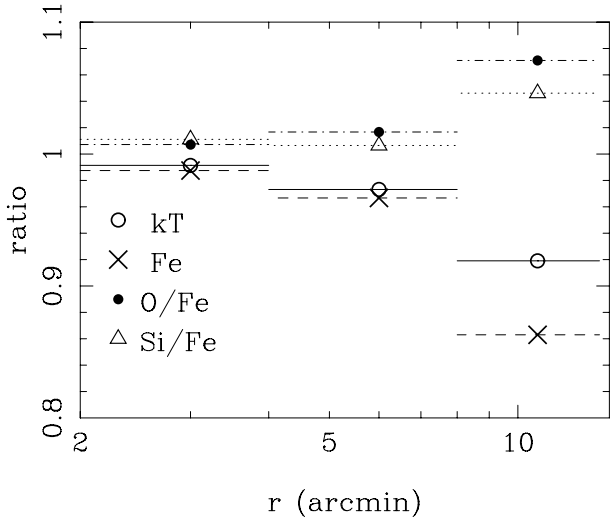

Fig. 8. The ratio of derived parameters of the projected EMOS spectra with the multi-temperature model using a background scaled by a factor of 1.1 to those using the unscaled background in the paper.

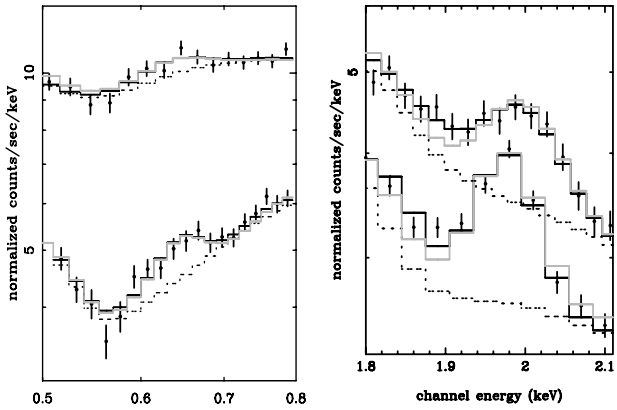

Fig. 9. Deprojected spectra of the EMOS (EMOS1+EMOS2; lower curve) and the EPN (upper curve) at $R = 2.0-8.0'$ around the energy of the lines of O (*left panel*) and Si (*right panel*). The gray data points and black solid lines correspond to the best-fit model with the one-temperature MEKAL model and the model with Gaussians with 0 line widths, respectively. The black dotted lines represent the continuum emissions as described by the Gaussian fit.

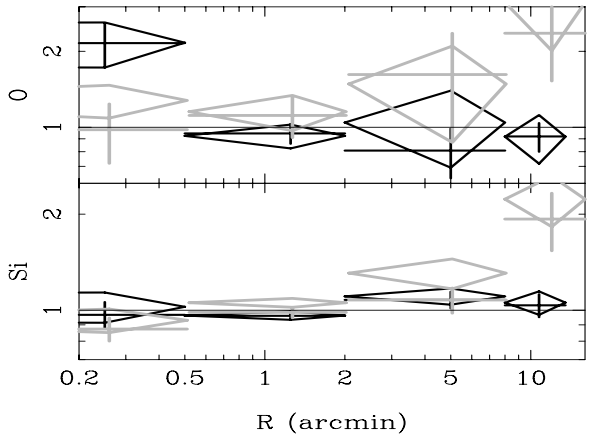

Fig. 10. The ratio of line strengths Kα of H-like O (*upper panel*) and Si (*lower panel*) derived from the Gaussian fit to those of best-fit values from the spectral fit for the EMOS (black lines) and EPN (gray lines). Crosses and diamonds correspond to the fitting with a Gaussian with 0 line width and free line width, respectively. Errors correspond the 68% level.

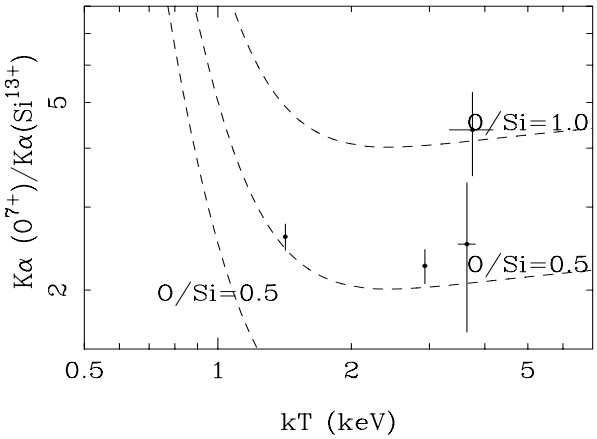

Fig. 11. The line ratios of Kα lines of H-like O and Si, for the projected spectra of the EMOS, plotted against the best-fit temperature fitted with the single MEKAL model. Dashed lines correspond to constant abundance ratios in units of the solar ratio. Errors represent the 68% confidence level.

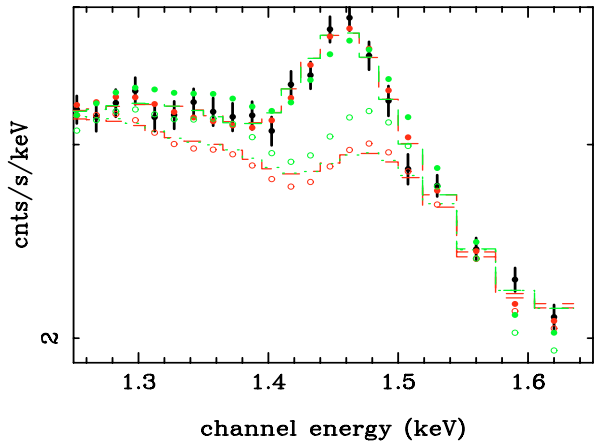

Fig. 12. The deprojected spectrum of the EMOS at $R = 0.5-2.0'$ (black closed circles) fitted with the multi-temperature MEKAL model (green closed circles), the multi-temperature APEC model (red closed circles), the Gaussians with MEKAL models (green dashed lines), and the Gaussians with the APEC models (red dashed lines). The contributions of the continuum plus the Fe-L are also shown for the multi-temperature APEC model (red open circles), the multi-temperature MEKAL model (green open circles) and the Gaussian fit (red and green dashed lines).

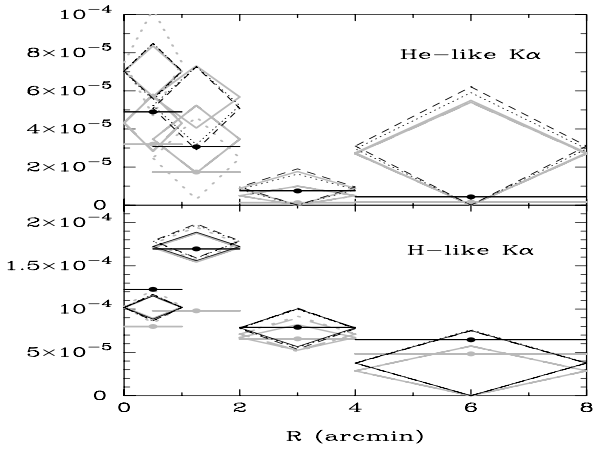

Fig. 13. The radial profile for the the Kα-line strength of He-like and H-like Mg for the best fit multi-temperature model (horizontal solid lines) and derived from the Gaussians plus a single temperature model (solid diamonds), two temperature model (dashed diamonds), and three-temperature model (dotted diamonds). The gray and black lines correspond to the MEKAL and APEC models, respectively. Errors correspond to a 68% confidence level.

those observed in center of other clusters and groups of galaxies, such as M 87 (Matsushita et al. 2003), A496 (Tamura et al. 2001a), Fornax cluster (Buote et al. 2002), and the group-center elliptical galaxies NGC 4636 (Xu et al. 2002), and NGC 5044 (Tamura et al. 2003; Boute et al. 2003). However, there are small differences in the observed abundance pattern of the ICM. For example, the central Fe abundance of the Centaurus cluster (2.3 solar) is 40% higher than that of M 87 (1.6 solar). In addition, the Si/Fe ratio of the former is 20% lower than that of the latter. In this section, we mainly compare and discuss the abundance pattern of the Centaurus clusters with that of M 87, since these two clusters are the nearest and the best-studied objects among relatively low-temperature clusters.

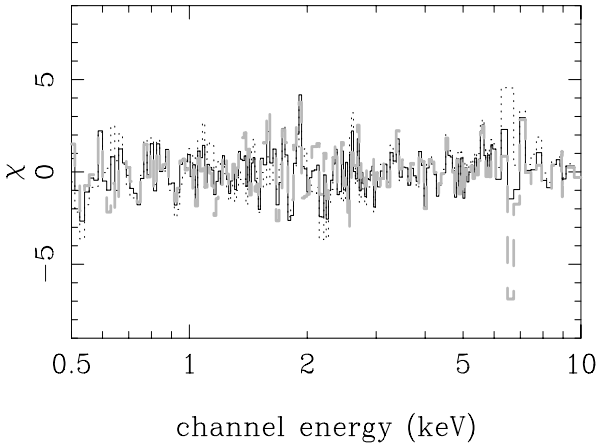

Fig. 14. The χ distributions of the deprojected spectrum at $R = 0.5-2.0'$ fitted with the multi-temperature APEC model. The solid black line corresponds to the best-fit model, and the dotted black line and dashed gray lines correspond to the model where the Fe abundance is fixed as 1.6 solar and 3.2 solar, respectively.

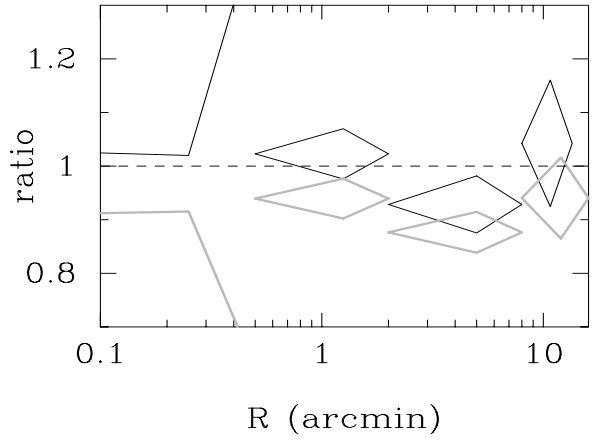

Fig. 15. The ratio of the line strengths of the 6.7 keV Fe-K line derived from the Gaussian fit to those of best-fit values from spectral fit for the EMOS (black lines) and EPN (gray lines), where the Fe-L is important for determining the Fe abundance. Errors correspond to the 68% level.

5.1. Comparison with stellar metallicity and SN II abundance pattern

The O and Mg in the gas around a cD galaxy is a mixture of those in the ICM and those in the accumulation of stellar mass loss from the cD galaxy, since these elements are only synthesized by SN II. The O and Mg abundances of the mass loss reflect those of mass-losing stars, which contribute significantly to the optical light from elliptical galaxies. The stellar metallicity of elliptical galaxies is usually derived from the Mg_2 index in the optical spectra, which mainly depends on the Mg abundance and stellar metallicity where O contributes most, and only weakly depend on the age population of stars. Therefore, comparing the O and Mg abundances of the gas and stellar metallicity derived from the optical Mg_2 index is important for studying the gas flow and contribution of stellar mass loss and stellar metallicity of the cD galaxies.

The Mg abundances of the two clusters are close to their stellar metallicity derived from the Mg_2 index (Fig. 16; Kobayashi & Arimoto 1999). The gradient of the Mg abundance of the gas around M 87 is steeper than in the Centaurus cluster. At a radius of 10–20 kpc, the Mg abundance of the Centaurus cluster is a

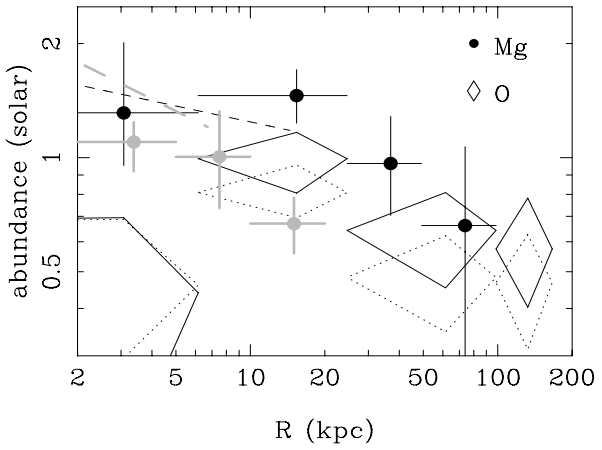

Fig. 16. Mg (closed circles) and O (diamonds) abundances derived for the Centaurus cluster (black) and M 87 (gray) from the multi-temperature MEKAL (dotted lines) and APEC (solid lines) model. The dashed lines represent the stellar metallicity of NGC 4696 (black) and M 87 (gray) derived from the optical Mg_2 index (Kobayashi & Arimoto 1999).

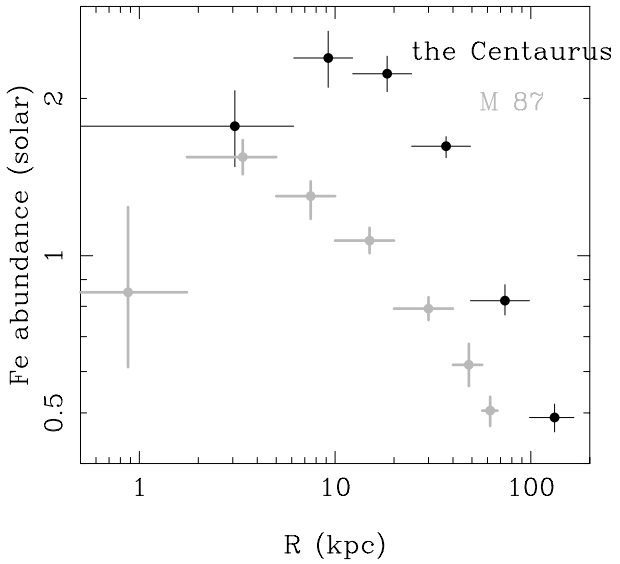

Fig. 17. The Fe abundance of the ICM of the center of Centaurus cluster (black) and M 87 (gray).

factor of 2 higher than that of M 87 (Fig. 16). The stellar metallicity gradient of M 87 is also steeper than for NGC 4696, the cD galaxy of the Centaurus cluster. The agreements between the Mg abundances with stellar metallicity in the central regions indicates that the gas in these regions is dominated by gas ejected from the cD galaxies.

The Mg/O ratio of the gas of the Centaurus cluster is 1.2 ± 0.3 of the solar ratio on average as determined with the multi-temperature APEC model. This is close to the value of the ICM within $4'$ of M 87, which is 1.3 ± 0.1 solar ratio (Matsushita et al. 2003), and also to the value of 1.3 ± 0.2 solar ratio of NGC 4636 (Xu et al. 2003) derived from the RGS. The observed Mg/O ratios of the gas at the cluster centers are close to [Mg/O] of the Galactic stars (Edvardsson et al. 1993). Therefore, the Galactic SN II and those trapped in stars in the cD galaxies are not different at least for the Mg/O ratio.

5.2. The Fe abundance profile and SN Ia contribution

The Fe in the gas in the core of clusters is also a mixture of those in the ICM and the recent supply from the cD galaxy, which contains Fe synthesized by SN Ia and those coming from stars through stellar mass loss, since Fe is synthesized by both SN Ia and SN II.

The Fe abundance of the ICM of the Centaurus cluster is systematically higher than around M 87 at the same distance from the cluster center (Fig. 17). The peak Fe abundance of the Centaurus cluster is 2.3 solar. This value is significantly higher than for M 87, which is 1.6 solar. Assuming that the O/Fe ratio of SN II is 3, the central Fe abundances from SN Ia of the Centaurus cluster and M 87 become 2 and 1.3 solar, respectively. Since the SN Ia contribution to the Fe abundance is dominant, the uncertainty in the assumption for the O/Fe ratio does not change the result very much.

The Fe abundance of gas from SN Ia in an elliptical galaxy is proportional to $M_{\rm SN}^{\rm Fe}\theta_{\rm SN}/\alpha_*$ (see Matsushita et al. 2003 for details). Here, $M_{\rm SN}^{\rm Fe}$ is the mass of Fe synthesized by one SN Ia, $\theta_{\rm SN}$ is SN Ia rate, and α_* is the stellar mass-loss rate. The higher Fe abundance of the gas in the central region of the Centaurus cluster indicates higher $M_{\rm SN}^{\rm Fe}\theta_{\rm SN}/\alpha_*$. The cooling flow rate derived from the standard cooling flow model is higher in the Centaurus cluster (Allen & Fabian 1994) than in the M 87 (Matsushita et al. 2002). Böhringer et al. (2004) question the standard cooling-flow model by comparing the Fe mass profile of 4 clusters of galaxies with cooling cores, including M 87 and the Centaurus cluster. They conclude that we need long enrichment times (>5 Gyr) in order to accumulate the observed Fe abundance peak even if the SN Ia rate was higher in the past.

As shown in Fig. 18, a difference between M 87 and the Centaurus cluster is the ratio of the Fe mass to the stellar *B*-band luminosity of the cD galaxy(IMLR). The total *B*-band luminosity and the effective radius were calculated using Prugniel & Heraudeau (1998), and the effect of the Galactic extinction was corrected using Schlegel et al. (1998). The IMLR of the Centaurus cluster is much higher than that of the M 87, especially within the central region. Since the contribution of the SN Ia to Fe in the ICM dominates, this indicates that the accumulation time scale of SN Ia is higher in the Centaurus cluster than in M 87, although we do not know the actual gas-flow rate due to the cooling flow problem. The longer accumulation time scale in the Centaurus cluster means that $M_{\rm SN}^{\rm Fe}\theta_{\rm SN}/\alpha_*$ was higher in the past. In other words, the Fe mass synthesized by a SN Ia was higher in the past or the ratio of SN Ia rate to the stellar mass-loss rate was higher in the past as suggested in Renzini et al. (1993).

5.3. Abundance pattern of SN Ia

Si is synthesized both by SN Ia and SN II, and the abundance pattern of O, Si, and Fe strongly constrains the nucleosynthesis of the SN Ia when Fe is dominated by SN Ia. Figure 19 summarizes the ratio of these three elements in the ICM of the Centaurus cluster and M 87 (Matsushita et al. 2003). As in M 87, the data of the Centaurus cluster cannot be explained by a sum of the SN II abundance pattern in the Galactic metal-poor stars (Clementini et al. 1999), and the SN Ia abundance pattern explained by the W7 model. The Si abundances are clearly higher than the sum of the two.

In the cluster center, the Fe/Si ratio and the Fe/O ratio of the gas of the Centaurus cluster are systematically higher than those of M 87, respectively. The main difference between M 87

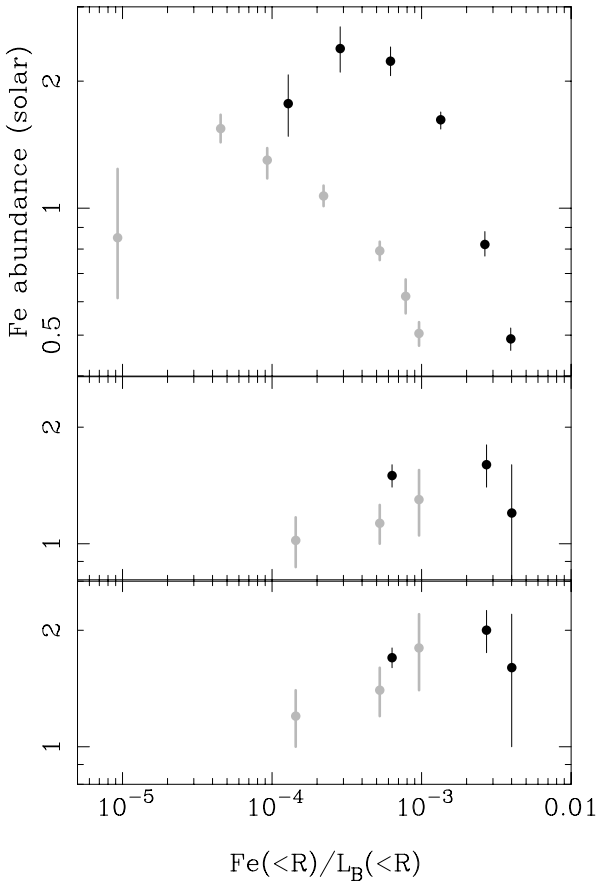

Fig. 18. The Fe abundance (the *upper panel*) and $(Fe/Si)_{SN\ Ia}$ (the *middle* and the *bottom panel*) in units of the solar values plotted against the ratio of the Fe mass to *B*-band luminosity of the cD galaxy (IMLR), for M 87 (gray circles) and the Centaurus cluster (black circles), when adopting the abundance pattern of SN II from the average value of Galactic metal poor stars (the *middle panel*; Clementini et al. 1999) and from nucleosynthesis model (the *bottom panel*) by Nomoto et al. (1997) assuming Salpeter's initial mass function (Iwamoto et al. 1999).

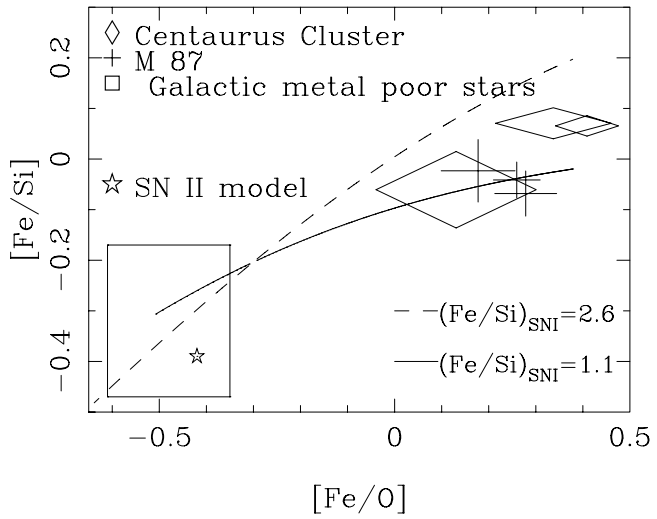

Fig. 19. [Fe/Si] of the ICM of the Centaurus cluster (diamonds) and M 87 (crosses; Matsushita et al. 2003) plotted against [Fe/O]. The average value of Galactic metal-poor stars (Clementini et al. 1999; open square) and the abundance ratio of SN II model using the nucleosynthesis model (asterisk) derived in Nomoto et al. (1997) are shown, assuming Salpeter's IMF (Iwamoto et al. 1999). The solid line and dashed line represent the relation of the abundance pattern synthesized by SN Ia with Fe/Si = 1.1 (the best-fit relation of M 87) and Fe/Si = 2.6 (W7 ratio; Nomoto et al. 1984), respectively.

and the Centaurus cluster is the IMLR as described in the previous section. In Fig. 18, $(Fe/Si)_{SN\ Ia}$ is also plotted against IMLR. The derived $(Fe/Si)_{SN\ Ia}$ value is much lower than the value of 2.6 in units of the solar ratio, which is predicted by the W7 model. Regions with higher IMLR have higher values of $(Fe/Si)_{SN\ Ia}$, when adopting the SN II pattern of either of the Galactic stars (Clementini et al. 1999) or of the nucleosynthesis model (Iwamoto et al. 1999), A higher IMLR corresponds to a longer accumulation time scale. For M 87, it needs only a few Gyr to accumulate the observed gas mass within 10 kpc where the gas from the cD galaxy dominates (Matsushita et al. 2002). In contrast, in the center of the Centaurus cluster, ejecta of SN Ia are accumulated over a much longer time scale than in M 87. Therefore, the correlation between $(Fe/Si)_{SN\ Ia}$ and IMLR support the suggestion by Finoguenov et al. (2002) and Matsushita et al. (2003) from observing M 87 that $(Fe/Si)_{SN\ Ia}$ depends on the age of the system. Matsushita et al. (2003) discovered that the Si/O ratio of the Galaxy also systematically increases toward metal-rich stars. This result indicates that there is a source of the high Si/O ratio in our Galaxy at present and supports the scenario suggesting a dependency on the Fe/Si ratio of ejecta of SN Ia on the age of the system.

5.4. The hydrogen column density and the cooling flow model

In the ASCA era, absorption within cluster cores was discussed in order to explain observed fluxes of soft energy photons that are much smaller than the expected value from the standard cooling flow model (Allen et al. 2001). To obscure a cooling flow in the Centaurus cluster from the standard model, we at least need additional column density around 2×10^{21} cm^{-2}. However, with the XMM-Newton observations, the observed hydrogen column density is too low to conceal the cool component from the cooling flow model (Matsushita et al. 2002; Böhringer et al. 2002). The observed hydrogen column density of the Centaurus cluster is also consistent with the Galactic value, 8.06×10^{20} cm^{-2} over the whole field of view. This means that the soft-energy photons from the Centaurus cluster are not obscured.

6. Conclusion

The abundance patterns of O, Mg, Si, and Fe of the ICM of the Centaurus cluster are derived with the XMM-Newton observation. At the very center, the Mg and O abundances are close to the stellar metallicity. This result indicates that the gas at the very center is dominated by the supply of the stellar mass loss from the cD galaxy.

The abundances of Si and Fe are close to each other in units of the solar abundance, while the O and Mg abundances are lower, as in the centers of other clusters and groups of galaxies. To explain the abundance pattern, the SN Ia ejecta from the cD galaxy should have a higher Si/Fe ratio than the standard W7 model by Nomoto et al. (1984).

There are small differences in the Fe abundances and the Fe/Si ratio in the ICM between the Centaurus cluster and M 87 (Matsushita et al. 2003). These differences and the higher IMLR in the Centaurus cluster may reflect a higher accumulation time scale of SN Ia. To confirm this suspicion, we will study

abundance patterns of the ICM of number of clusters and groups of galaxies further with Suzaku, which has a better energy resolution at the O lines.

Acknowledgements. This work was supported by Humboldt foundation. The paper is based on observations obtained with XMM-Newton, an ESA science mission with instruments and contributions direct by funded by ESA Member States and the USA (NASA). The XMM-Newton project is supported by the Bundesministerium für Bildung und Forschung, Deutsches Zentrum für Luft und Raumfahrt (BMBF/DLR), the Max-Planck Society, and the Haidenhain-Stiftung.

References

Allen, S. W., & Fabian, A. C. 1994, MNRAS, 269, 409
Allen, S. W., Fabian, A. C., Johnstone, R. M., Arnaud, K. A., & Nulsen, P. E. J. 2001, MNRAS, 322, 589
Böhringer, H., Belsole, E., Kennea, J., et al. 2001, A&A, 365, L181
Böhringer, H., Matsushita, K., Churazov, E., et al. 2002, A&A, 382, 804
Böhringer, H., Matsushita, K., Churazov, E., et al. 2004, A&A, 416, L21
Buote, D. A., Jeltema, T. E., Canizares, C. R., et al. 2002, ApJ, 577, 183
Buote, D. A., Lewis, A. D., Brighenti, F., et al. 2003, ApJ, 595, 151
Clementini, G., Gratton, R. G., Carretta, E., et al. 1999, MNRAS, 302, 22
Edvardsson, E., Andersen, J., Gustafsson, B., et al. 1993, 275, 101
Feldman, U. 1992, Phys. Scr., 46, 202
Finoguenov A., Matsushita, K., Böhringer, H., et al. 2002, A&A, 381, 21
Fukazawa, Y., Ohashi, T., Fabian, A. C., et al. 1994, PASJ, 46, L55
Hamuy, M., Philips, M. M., Suntzeff, N. B., et al. 1996, AJ, 112, 2438
Ikebe, Y., Makishima, K. Fukazawa, Y., et al. 1999, ApJ, 525, 58
Iwamoto, K., Brachwitz, F., Nomoto, K., et al. 1999, ApJS, 125, 439
Ivanov, V., Hamuy, M., & Pinto, P. A. 2000, ApJ, 542, 588
Kaastra, J. S. 1992, An X-Ray Spectral Code for Optically Thin Plasmas (Internal SRON-Leiden Report)
Katayama, H., Takahashi, I., Ikebe, Y., Matsushita, K., & Freyberg, M. 2004, A&A, 414, 767
Kirsh 2002, XMM-cal-report
Kobayashi, C., & Arimoto, N. 1999, ApJ, 527, 573
Liedahl, D. A., Osterheld, A. L., & Goldstein, W. H. 1995, ApJ, 438, L115
Makishima, K., Ezawa, H., Fukazawa, Y., et al. 2001, PASJ, 53, 401
Matsushita, K., Belsole, E., Finoguenov, A., & Böhringer, H. 2002, A&A, 386, 77
Matsushita, K., Finoguenov, A., & Böhringer, H. 2003, A&A, 401, 443
Nomoto, K., Thielemann, F.-K., & Yokoi, K. 1984, ApJ, 286, 644
Nomoto, K., Hashimoto, M., Tsujimoto, T., et al. 1997, Nucl. Phys. A, 616, 79
Nugent, P., Baron, E., Branch, D., et al. 1997, ApJ, 485, 812
Prugniel, P., & Heraudeau, P. 1998, A&AS, 128, 299
Renzini, A., Ciotti, L., D'Ercole, A., et al. 1993, ApJ, 419, 52
Sanders, J. S., & Fabian, A. C. 2002, MNRAS, 331, 273
Schlegel, D. J., Finkbeiner, D. P., & Davis, M. 1998, ApJ, 500, 525
Smith, R. K., Brickhouse, N. S., Liedahl, D. A., & Raymond, J. S. 2001, ApJ, 556, 91
Takahashi, I. 2004, Ph.D. Thesis, University of Tokyo
Tamura, T., Bleeker, J. A. M., Kaastra, J. S., et al. 2001a, A&A, 379, 107
Tamura, T., Kaastra, J. S., Peterson, et al. 2001b, A&A, 365, L87
Tamura, T., Kaastra, J. S., Makishima, K., & Takahashi, I. 2003, A&A, 399, 497
Umeda, H., Nomoto, K., & Kobayashi, C. 1999, ApJ, 522, L43
Xu, H., Kahn, S. M., Peterson, J. R., et al. 2002, ApJ, 579, 600